Published in final edited form as:
Acta Neuropathol. 2022 March ; 143(3): 331–348. doi:10.1007/s00401-021-02393-1.

Perivascular Space Dilation is Associated with Vascular Amyloid-β Accumulation in the Overlying Cortex

Valentina Perosa, MD[*,1,2,3], Jan Oltmer[4], Leon P. Munting, PhD[5,6], Whitney M. Freeze, PhD[6,7], Corinne A. Auger, BM[5], Ashley A. Scherlek, BM[5,8], Andre J. van der Kouwe, PhD[4], Juan Eugenio Iglesias, PhD[4,9,10], Alessia Atzeni[9], Brian J. Bacskai, PhD[5], Anand Viswanathan, MD PhD[1], Matthew P. Frosch, MD PhD[5,11], Steven M. Greenberg, MD PhD[1], Susanne J. van Veluw, PhD[1,5,6]

[1]J. Philip Kistler Stroke Research Center, Department of Neurology, Massachusetts General Hospital, Harvard Medical School, Boston, MA, USA

[2]Department of Neurology, Otto-von-Guericke University, Magdeburg, Germany

[3]German Center for Neurodegenerative Diseases (DZNE), Magdeburg, Germany

[4]Athinoula A. Martinos Center for Biomedical Imaging, Department of Radiology, Massachusetts General Hospital and Harvard Medical School, Charlestown, MA, USA

[5]MassGeneral Institute for Neurodegenerative Disease, Massachusetts General Hospital, Charlestown, MA, USA

[6]Department of Radiology, Leiden University Medical Center, Leiden, the Netherlands

[7]Department of Neuropsychology and Psychiatry, Maastricht University, Maastricht, the Netherlands.

[8]Rush Alzheimer Disease Center, Rush University Medical Center, Chicago, IL, USA

[9]Centre for Medical Image Computing, University College London, London, United Kingdom

[10]Computer Science and Artificial Intelligence Laboratory, Massachusetts Institute of Technology, Cambridge, MA, USA

[11]Neuropathology Service, C.S. Kubik Laboratory for Neuropathology, Massachusetts General Hospital, Harvard Medical School, Boston, MA, USA

Abstract

Perivascular spaces (PVS) are compartments surrounding cerebral blood vessels that become visible on MRI when enlarged. Enlarged PVS (EPVS) are commonly seen in patients with cerebral

---

[*] Corresponding author: Valentina Perosa, MD, J. Philip Kistler Stroke Research Center, Massachusetts General Hospital, Cambridge Str. 175, Suite 300; Boston, MA 02114, USA, Tel: +1 8572631663; Fax: +1 617-726-5043, VPEROSA@mgh.harvard.edu.

Author contributions

V.P. and S.J.v.V. designed the study. S.M.G. and A.V. supported data collection. C.A.A. and A.A.S. processed histopathological material. A.J.v.d.K. provided support in optimizing the scanning parameters. Data was analyzed by V.P. with support from J.O., J.E.I.G., W.M.F. and A.A. V.P. and S.J.v.V. drafted the manuscript and all authors reviewed it and provided feedback. The project was supervised by S.J.v.V.

Competing interests

The authors declare no competing interests.

small vessel disease (CSVD) and have been suggested to reflect dysfunctional perivascular clearance of soluble waste products from the brain. In this study, we investigated histopathological correlates of EPVS and how they relate to vascular amyloid-β (Aβ) in cerebral amyloid angiopathy (CAA), a form of CSVD that commonly co-exists with Alzheimer's disease (AD) pathology. We used *ex vivo* MRI, semiautomatic segmentation and validated deep learning-based models to quantify EPVS and associated histopathological abnormalities. Severity of MRI-visible PVS during life was significantly associated with severity of MRI-visible PVS on *ex vivo* MRI in formalin fixed intact hemispheres and corresponded with PVS enlargement on histopathology in the same areas. EPVS were located mainly around the white matter portion of perforating cortical arterioles and their burden was associated with CAA severity in the overlying cortex. Furthermore, we observed markedly reduced smooth muscle cells and increased vascular Aβ accumulation, extending into the WM, in individually affected vessels with an EPVS. Overall, these findings are consistent with the notion that EPVS reflect impaired outward flow along arterioles and have implications for our understanding of perivascular clearance mechanisms, which play an important role in the pathophysiology of CAA and AD.

Keywords

cerebral amyloid angiopathy; cerebral small vessel disease; clearance; ex vivo MRI; enlarged perivascular spaces

Introduction

Perivascular spaces (PVS) [12], are compartments that surround cerebral blood vessels [47]. When enlarged, PVS become visible on T2-weighted MRI as hyperintense elongated structures [67, 69], which in this study are referred to as MRI-visible PVS [5]. The presence of MRI-visible PVS has been associated with ageing [57], hypertension [66], stroke [24] and cognitive impairment [62]. Furthermore, MRI-visible PVS have been increasingly recognized as a hallmark neuroimaging manifestation of cerebral small vessel disease (CSVD), the leading cause of intracerebral hemorrhage in older individuals [70] and a contributing factor to dementia [11, 32, 49].

The exact mechanisms leading to the enlargement of PVS have not yet been fully elucidated. It has been suggested that fluid accumulation in the PVS occurs due to an impairment of perivascular brain clearance [12, 41]. Increasing evidence suggests that soluble waste products are cleared from the brain along PVS [1, 31] and that pathological changes in the walls of blood vessels (such as arteriosclerosis, lipohyalinosis, and vascular amyloid β (Aβ) accumulation), cause impairment in perivascular clearance [36, 65, 71]. At the same time, dysfunction of perivascular clearance may limit effective waste removal from the brain [4, 52, 68], including Aβ [38] and tau [31], which might further accelerate vascular Aβ accumulation and thus dysfunction of perivascular clearance in a vicious cycle. The imbalance between production and clearance of Aβ and tau is thought to be a leading mechanism in the development of neurodegenerative diseases, such as Alzheimer's disease (AD) [63] and cerebral amyloid angiopathy (CAA) [25]. Many questions, related to the anatomical routes, driving forces, and directionality of perivascular clearance remain.

Unraveling the neuropathological correlates of PVS enlargement may yield important new insights in this regard.

In CAA, Aβ accumulates in the walls of cortical and leptomeningeal arteries, resulting in a loss of smooth muscle cells and impaired vascular function [25]. CAA can lead to intracerebral hemorrhage and cognitive impairment in the elderly [15] and is found in 50% to 80% of patients with AD [33, 50]. MRI-visible PVS in the juxtacortical white matter (WM) of the centrum semiovale (CSO) are a prominent neuroimaging feature of CAA and are related to disease severity [16]. A link between cortical vasculopathy and enlargement of PVS in the underlying WM has been previously suggested in a pathological study, that included cases with AD [54] and in a pilot histopathological study on cases with CAA [64]. It has been hypothesized, that the mechanism behind this link is impaired perivascular clearance [26], for example due to vascular Aβ accumulation in the cortical vessels, which leads to clearance impairment along these vessels and thus to fluid stagnation and enlargement of PVS along connected perivascular compartments in the WM portion of the same vessels. The overarching objective of this study was to test this assumption, using detailed MRI-guided histopathological examination of MRI-visible PVS in CAA patients. More specifically, we addressed the following hypotheses: i) the histopathological substrate of MRI-visible PVS is an enlargement of the perivascular compartment; ii) the severity of PVS enlargement is associated with the severity of CAA in the overlying cortex, independent of other pathological alterations; iii) the EPVS-related vessels in the juxtacortical WM are the same perforating cortical arteries affected by CAA.

Materials and Methods

Cases

We included nineteen autopsy cases with pathologically confirmed CAA and five non-CAA control cases from an ongoing brain autopsy program that aims to evaluate MRI markers of clinically diagnosed CAA and their underlying histopathology. The program was initiated in 2015 within the stroke research center at MGH and includes brain donations that came through MGH and outside hospitals [66]. Study approval was received from the MGH institutional review board (protocol number: 2021P001920), according to the declaration of Helsinki, and informed consent was obtained from the next of kin or another legal representative prior to autopsy. After autopsy, the most intact cerebral hemisphere was fixed in 10% formalin for several weeks and subjected to *ex vivo* 3 tesla MRI scanning and histopathological examination, while the other hemisphere underwent routine neuropathological examination by a board-certified neuropathologist. If available, *in vivo* MRI scans were requested from outside hospitals.

Ex vivo MRI

Details of *ex vivo* MRI scanning have been previously described [66]. Briefly, hemispheres were vacuum-sealed in a plastic bag containing periodate-lysine-paraformaldehyde, placed in the 32-channel head coil of a whole-body 3 tesla MRI scanner (MAGNETOM Trio, Siemens Healthineers, Erlangen, Germany) and scanned overnight. The protocol included several sequences, including a T2-weighted turbo-spin echo (TSE) sequence (echo time 61 ms, repetition time 1800 ms, flip angle 150°, voxel size 500 × 500 × 500 μm isotropic, 1 average, total scan time ~3 hours), which was used in this study.

Histopathology

After scanning, the hemispheres were cut in 1 cm-thick coronal slabs. Samples were cut from five pre-defined standard areas: four including cortex and juxtacortical white matter (from the frontal, temporal, parietal, and occipital lobe) and one from the basal ganglia (BG). All sampled tissue blocks were processed and embedded in paraffin and 6 μm-thick sections were cut with a microtome. Sections were stained using hematoxylin & eosin (H&E) and luxol fast blue with H&E (LHE), following standard histology protocols. Bright field immunohistochemistry against Aβ (mouse, clone 6F/3D; Agilent Technologies, Santa Clara, CA; 1:200, Cat# M0872) and fibrin(ogen) (rabbit, Dako Carpinteria, CA; 1:500, Cat# A0080) was performed as previously described [66]. Briefly, following a standardized immunohistochemistry protocol, sections were deparaffinized and rehydrated through xylene and graded ethanol series. Next, endogenous peroxidase was blocked with 3% H_2O_2 (20 min), followed by formic acid treatment (for Aβ, 5 min) or antigen retrieval in heated citrate buffer (for fibrinogen). Tissue was then blocked with normal horse or goat serum (1 hour) and incubated overnight with the primary antibody at 4°C. On the next day, the biotinylated mouse or rabbit secondary antibody was applied (1 hour), followed by a mixture of avidin (A) and biotinylated HRP (B) (Vectastain ABC kit, Vector laboratories, 30 min) and 3,3'-Diaminobenzidine (DAB, Vector laboratories).

Histopathological image analysis

Stained sections were scanned using a Hamamatsu NanoZoomer Digital Pathology (NDP)-HT whole slide scanner (C9600–12, Hamamatsu Photonics KK, Japan), with a 20x objective. Obtained high-resolution (457 nm/pixel; 55579 dpi) digital images were visualized using the NDP.view2 software (version 2.8.24). In order to obtain continuous measures for the severity of PVS enlargement, the area occupied by EPVS was semi-automatically segmented, using an in-house developed tool with ImageJ (v. 2.1.0./1.53c) [58]. The WM was manually segmented on the LHE-stained sections. In the BG sections, both the WM and the subcortical nuclei were segmented. For simplicity we here refer to the whole area as WM. The image was then converted into 8-bit grey values after which the EPVS were segmented by setting an image specific threshold based on mean grey value of the tissue, after excluding the background (mean gray value – 2 * standard deviation). Each image was visually inspected and any artefactual tissue alterations caused by tissue processing and/or staining were manually excluded from the segmentation. The number of pixels occupied by the EPVS as well as by the whole WM was then extracted, to obtain percentage EPVS area of total WM area: [EPVS (px)/total WM (px)] *100.

Quantitative measures of the sections stained for Aβ and Fibrin(ogen) were obtained using the online platform Aiforia®. Details of the method have been described elsewhere [46]. Briefly, sections were uploaded on the Aiforia® platform and annotations (ground truth) were manually drawn on 10% of the dataset, in order to train convolutional neural networks (CNNs). Once trained, the AI-models were applied to the whole dataset and both visual quality control and validation were performed, in order to ensure their adequate performance. More specifically, validation of each CNN was implemented on a subset of approximately 10% of sections, different from those on which the model had been trained. Within randomly drawn validation regions, the marker of interest was annotated by three independent and trained human validators. The percentage of false positives (FP), false negatives (FN), precision (TP/[TP+FP]), sensitivity (TP/[TP+FN]) and F1-score (2 x Precision x Sensitivity/[Precision + Sensitivity]) for each CNN versus each human validator were obtained for all validation regions and subsequently averaged across all validators. Precision, sensitivity, and F1-score were good (> 80%) to excellent (> 90%) for all relevant measures.

Results for cortical grey matter and white matter (WM) respectively were obtained by manually segmenting the sections on the Aiforia® platform into regions of interest, guided by the adjacent LHE-stained sections, which provide excellent contrast between grey and white matter.

Two AI-models and the following derived measures were adopted for this study: 1) Aβ model: percentage area of leptomeningeal CAA (leptomeningeal CAA area [mm^2]/ leptomeningeal tissue area [mm^2]); percentage area of cortical CAA (cortical CAA area [mm^2]/cortical tissue area [mm^2]); total CAA percentage area (cortical CAA area [mm^2] + leptomeningeal CAA area [mm^2]/ cortical tissue area [mm^2] + leptomeningeal tissue area [mm^2]); percentage area of Aβ-plaques (cortical Aβ-plaques area [mm^2]/cortical tissue area [mm^2]). 2) Fibrin model: percentage area of fibrin positive blood vessels in the WM (fibrin positive vascular WM tissue area [mm^2]/WM tissue area [mm^2] + fibrin positive vascular WM tissue area [mm^2]). After quality control, few sections had to be excluded from the analyses, due to suboptimal performance of the AI-models (four for the measurements derived from the Aβ model, three for the ones derived from the fibrin model) (See [46] for details). The mean integrated density of the WM was calculated using ImageJ on the LHE-stained sections after subtracting the area occupied by the EPVS as a measure of myelin rarefaction.

In vivo and ex vivo MRI assessment

The available clinical axial T2-weighted sequences were obtained at 3 tesla with one of the following set of parameters: 1) voxel size 0.7 × 0.7 × 5 mm, flip angle = 150°, repetition time = 3000 ms, echo time = 86 ms, bandwidth = 191 Hz/px; 2) voxel size 0.5 × 0.5 × 5 mm, flip angle = 120°, repetition time = 7060 ms, echo time = 85 ms, bandwidth = 260 Hz/px; 3) voxel size 0.5 × 0.5 × 2 mm, flip angle = 60°, repetition time = 7500 ms, echo time = 84 ms, bandwidth = 286 Hz/px. According to established criteria [48], the severity of MRI-visible PVS was assessed in axial orientation at the level of the BG and CSO, on available T2-weighted *in vivo* clinical MRI scans. Briefly, EPVS were defined as hyperintense stripes measuring < 3 mm and were screened on up to three randomly selected slices of the BG and CSO, within the same hemisphere that was chosen for *ex vivo* MRI. One slice in the CSO and one slice in the BG with the most MRI-visible PVS was selected and formally rated according to the following semiquantitative score: 0, absence (no MRI-visible PVS); 1, mild (1 – 10 MRI-visible PVS); 2, moderate (11 – 20); 3, frequent (21 – 40); 4, severe (> 40). The same procedure was adopted to assess MRI-visible PVS on the *ex vivo* T2-weighted MRI (Fig. 1; Supplementary Fig. 1). The width of each MRI-visible PVS on *in vivo* and *ex vivo* MRI was assessed on a single CSO slice in two cases that underwent *in vivo* MRI with identical parameters and had available co-registered *in vivo* and *ex vivo* MRI scans (case no. 5 and no. 13). Measurements and registration were performed with *freeview,* integrated within FreeSurfer v7.1.0 (http://surfer.nmr.mgh.harvard.edu/).

Furthermore, severity of MRI-visible PVS was assessed regionally on *ex vivo* MRI in the BG and the four juxtacortical WM regions that were included in the sampled areas (from the frontal, temporal, parietal, and occipital lobes) that underwent subsequent histopathological evaluation. The T2-weighted TSE sequence was inspected in coronal orientation and matched to the corresponding histopathological section, guided by anatomical landmarks and photographs of the sampled areas (Fig. 2). The following semiquantitative score was applied: 0, absence (no MRI-visible PVS); 1, mild (1 – 5 MRI-visible PVS); 2, moderate (6 – 10); 3, severe (> 10) (Supplementary Fig. 2). MRI ratings were performed by V.P. (MD, neurologist with 6 years of experience) blinded to clinical diagnosis. A second rater J.O. (MD, with 2 years of experience in neuroimage analysis) assessed the images as well to determine inter-rater reliability. MRI scans were visualized with MeVisLab, Version 3.1.1 (MeVis, Bremen, Germany). In order to account for the known association between hypertension and MRI-visible PVS in the BG [24], diagnoses of arterial hypertension during life was extracted from available medical records.

Ultra-high resolution ex vivo MRI

In order to perform an in-depth characterization of the morphology of MRI-visible PVS and the PVS-related vessels, ultra-high resolution *ex vivo* 7 tesla MRI and serial sectioning were performed on two tissue samples selected from two CAA cases. Available *in vivo* MRI scans were assessed to identify two scans with identical acquisition parameters for the T2-weighted axial sequence and different degrees of severity of MRI-visible PVS. One case with mild (no. 5, grade 2) and one with severe MRI-visible PVS in the CSO (no. 13, grade 4) were selected, and a tissue block of 2.5 × 4 × 1 cm was cut from the parietooccipital region. The tissue blocks were first placed in phosphate-buffered saline for 24 hours (to restore relaxation parameters), then wedged in a 50 mL Falcon tube filled with Fomblin® (Solvay Solexis), which was sealed after air bubbles were carefully removed. The scan was performed overnight at a 7 tesla Siemens MAGNETOM whole-body MRI, using a custom-made solenoid coil with an inner diameter of 30 mm. The protocol included a T2-weighted TSE sequence with the following parameters: matrix 320 × 512, 128 partitions, voxel size 100 × 100 × 100 μm isotropic, 32 × 51.2 × 12.8 mm volume, flip angle = 120°, turbo factor = 9, repetition time = 1500 ms, echo time = 79 ms, bandwidth = 148 Hz/px (dwell 6600 ns), 4 averages, total scan time ~8 hours. A fast low angle shot (FLASH) sequence was also acquired with the following parameters: four runs each of four flip angles (10°, 20°, 30°, and 40°), matrix 448 × 896, 352 partitions, voxel size 75 × 75 × 75 μm isotropic, 33.6 × 67.2 × 26.4 mm volume, repetition time = 45 ms, echo time = 15.8 ms, bandwidth = 70 Hz/px, 4 averages, total scan time ~ 4 hours.

The scans of these blocks were rigidly registered to the space of the *in vivo* and *ex vivo* 3 tesla MRI scans. Registration was manually initialized and then automatically optimized with *mri_robust_register*, [53] integrated within FreeSurfer v7.1.0 (http://surfer.nmr.mgh.harvard.edu/). Next, deep learning was used to segment MRI-visible PVS on the averaged ultra-high resolution T2-weighted sequence. For this, ground truth was produced by manually labelling the MRI-visible PVS on a total of eight sub-volumes. These subvolumes and their corresponding manual labels were used to train a 3D Unet [20, 56] for automated segmentation of MRI-visible PVS, which was subsequently applied to the whole volume. Due to the limited availability of data, an architecture with three resolution levels of two layers each was adopted. Each layer had sixteen feature maps. Convolutions were performed with kernels of size 3 × 3 × 3. We used the exponential linear unit as activation [21]. The last layers used a softmax activation function. We used soft Dice as loss function [44]. The lack of training data was further mitigated with data augmentation, both geometric (random rotations, scaling, shearing, and nonlinear deformation) and of the image intensities (brightness, contrast, and gamma transforms), all computed on the fly for every minibatch.

Furthermore, WM and GM were also segmented semi-automatically with an existing open-source tool, named *SmartInterpol* [3]. Specifically, the GM and WM were manually labeled every twentieth slice in each block, and *SmartInterpol*, which combines CNNs with multi-atlas segmentation [30, 55], was used to compute the segmentation for the rest of the slices. Using an in-house developed MATLAB code (2017b, Mathworks), we split the MRI-visible PVS segmentation into individual MRI-visible PVS using connected component analysis, and used the output of *SmartInterpol* to separate the MRI-visible PVS into those visible in the WM and those protruding into the GM. Finally, we computed the ratio between number of MRI-visible PVS in GM / number of MRI-visible PVS in WM.

Serial sections

The two samples that underwent ultra-high resolution *ex vivo* MRI were then cut in half to fit standard tissue cassettes and embedded in paraffin. 6 μm thick serial sections were obtained with the microtome and each twentieth section successively stained for H&E. Immunohistochemistry was performed on adjacent sections for Aβ and for smooth muscle actin (SMA) (mouse, Dako, 1:250, Cat# M0851), following the protocol described above. Four sections from each of the two blocks were randomly chosen from the H&E-stained serial sections. All WM vessels with a diameter > 10 μm were selected, numbered and classified as related to an EPVS (when the space, measured perpendicular to the vessel over the full length of the space, was as wide as 30% of the vessel's diameter or above) or not related to an EPVS. The chosen H&E-stained sections were at least 120 μm apart and longitudinally cut vessels were considered only once, to avoid/minimize counting a vessel twice. The same vessels were rated on the adjacent Aβ-stained sections for presence or absence of Aβ in the vessel wall, blinded to H&E. Finally, the same vessels were classified on the adjacent SMA-stained sections as arterioles or venules, according to the presence or absence of SMA-positive cells in the vessel wall (Supplementary Fig. 3). Vessels that could not be found on the adjacent sections were excluded from the analysis.

Quantification of EPVS in hereditary CAA

In order to determine whether our observations in sporadic CAA also applied to hereditary CAA, a parietooccipital block of tissue from a case (Female; Age at death = 51 y) with Dutch-type hereditary CAA (D-CAA, also referred to as cerebral hemorrhage with amyloidosis-Dutch type, HCHWA-D) [41] was included in the analyses. The tissue block was obtained from a brain of the neuropathology tissue collection of the Leiden University Medical Center, the Netherlands. Written informed consent was obtained from this donor and data were handled in a coded fashion maintaining patient anonymity according to Dutch national ethical guidelines (Code for Proper Secondary Use of Human Tissue, Dutch Federation of Medical Scientific Societies, Rotterdam, the Netherlands). Ultra-high resolution *ex vivo* 7 tesla MRI, serial sections, and related quantifications were performed on this tissue block exactly as described above.

Statistical analysis

Statistical analyses were performed using the software R, version 3.6.0 (R Foundation for Statistical Computing, Vienna, Austria; www.R-project.org) and the Statistical Package for Social Science (IBM SPSS Statistics), version 25. Graphics were created with GraphPad Prism version 9.0.2, R version 3.6.0 and BioRender (www.biorender.com).

A Chi-squared-test was used to assess differences in frequency of hypertension between CAA and non-CAA groups. Partial Spearman rank-order correlation coefficients were calculated to establish the relationship between: a) MRI-visible PVS on *in vivo* and *ex vivo* MRI, adjusting for the interval between *in vivo* MRI and time-of-death; b) *ex vivo* regional score of MRI-visible PVS and percentage area of EPVS on histopathology; c) percentage area of CAA in the WM and percentage EPVS area within CAA cases; d) average percentage of EPVS area on histopathology in each case and *post-mortem* interval. For this purpose, the “ppcor” package version 1.1 for R was adopted. Data were tested for violation of normality using Shapiro-Wilk tests. A non-parametric Mann-Whitney U test was used to compare MRI-visible PVS severity, as well as percentage EPVS area between CAA and non-CAA cases. Wilcoxon signed-rank test served to determine differences in the diameter of MRI-visible PVS *ex vivo* and *in vivo*.

To test whether CAA was a predictor of the severity of PVS enlargement on histopathology, we fitted linear mixed effects (LME) models, using the “lme4” package version 1.1–26 in R [6]. In all models, percentage EPVS area was set as dependent variable, while subject and cortical region (frontal, temporal, parietal, and occipital) were defined as random factors, in this way accounting for subject- and region-dependent differences in pathology. First, we fitted a null (0) model, including age at death and sex. Subsequently, we constructed two sets of models setting total percentage area of CAA (1a) and a model with both percentage area of cortical and leptomeningeal CAA (1b) as fixed factors. We then added respectively further fixed factors as a proxy of other pathological markers hypothesized to be potential contributors: percentage area of fibrin positive blood vessels in the WM (as a measure of BBB-leakage) (2a; 2b), myelin rarefaction (3a; 3b), and percentage area of cortical Aβ-plaques (as a measure of AD pathology) (4a; 4b). Finally, we fitted two “comprehensive models” with all these predictors (5a; 5b). We compared the model fit using likelihood ratio test and evaluating the change in Akaike information criterion (AIC) and Bayesian information criterion (BIC). For both indexes, a smaller value indicates a better fit. Chi square tests were used to calculate the difference in expected and observed frequencies for the presence of EPVS, and to determine whether presence of Aβ in the WM portion of the vessel wall and the type of vessel (i.e. arteriole or venule) were associated with the presence of EPVS around WM vessels. A p-value of < 0.05 was considered statistically significant, and tests were always two-tailed.

Results

In vivo burden of MRI-visible PVS is associated with burden on ex vivo MRI

Nineteen cases with definite CAA (median age at death = 74 years; range = 64 – 88 years) and five non-CAA control cases (median age at death = 88 years; range = 82 – 95 years) were included in this study (Table 1). Clinical *in vivo* and research *ex vivo* MRI scans were visually assessed, to compare MRI-visible PVS burden between CAA cases and controls and to assess whether PVS severity during life was preserved in the fixed brain tissue of the same individuals *post-mortem*. Clinical *in vivo* MRI scans with an axial T2-weighted sequence were available for 17/19 CAA cases and 4/5 control cases. MRI scans were acquired with a median of 21 months (range 7 – 70 months) prior to death for the non-CAA group and 18 months (range 5 – 157 months) prior to death for the CAA group (Mann-Whitney U = 862.5, p = 0.922). There was no difference in frequency of hypertension between groups (Chi-squared = 0.064, p = 0.800). Inter-rater reliability was calculated using the intraclass correlation coefficient (ICC) for the MRI-visible PVS and proved to be very good to excellent for both the *in vivo* (0.89) and for the *ex vivo* scans (0.75).

On *in vivo* and *ex vivo* MRI, the degree of MRI-visible PVS in the CSO was more severe in CAA cases compared to non-CAA cases (*in vivo*: Mann-Whitney U = 225.0, p < 0.001; *ex vivo*: Mann-Whitney U = 587.5, p = 0.016). In the BG, no difference was observed between groups *in vivo* (Mann-Whitney U = 650, p = 0.083), while on *ex vivo* MRI, CAA cases had a higher degree of MRI-visible PVS in the BG than non-CAA cases (Mann-Whitney U = 1112.5, p = 0.015). The degree of MRI-visible PVS assessed on *in vivo* MRI in the CSO and BG respectively was positively associated with severity assessed on *ex vivo* MRI (CSO: Spearman’s ρ = 0.58, p < 0.001; BG: Spearman’s ρ = 0.20, p = 0.039), when corrected for *in vivo* MRI-time-of-death interval. When excluding the case with a 157-month interval between *in vivo* MRI and time-of-death, the correlation in the BG but not the CSO attenuated (p = 0.164).

A total of n=78 MRI-visible PVS was measured on the *in vivo* MRI and on the corresponding *ex vivo* T2 sequence of two cases (no. 5 and no. 13) with coregistered MRI. A difference between the width of MRI-visible PVS *in vivo* (median = 0.94mm; range = 0.36 – 1.76mm) and *ex vivo* (median = 0.86mm; range = 0.40 – 1.29mm) was found (V = 2057, p-value = 0.002). Examples of the MRI scans are shown in Fig. 1 and Supplementary Fig. 1. Collectively, we confirmed previous reports of higher degree of MRI-visible PVS in the CSO, but not the BG, in CAA cases compared to non-CAA controls [16]. Moreover, importantly *ex vivo* MRI seemed to consistently capture degree of PVS after a period of formalin fixation.

Regional MRI-visible PVS severity on ex vivo MRI correlates with EPVS area on histopathology

On histopathology, MRI-visible PVS corresponded to enlarged spaces surrounding blood vessels in the WM. Notably, the majority of spaces appeared not to be completely empty, but to contain cells as well as extracellular matrix with reticular appearance and occasionally hemosiderin deposits (Supplementary Fig. 2). Next, we quantified regional severity of juxtacortical PVS both on *ex vivo* 3 tesla MRI and on the LHE-stained sections for all (n = 25) cases and controls and in all sampled regions (frontal, temporal, parietal, occipital, and BG; n = 120 samples in total). Regional score of MRI-visible PVS on *ex vivo* 3 tesla MRI was positively associated with percentage of EPVS area on histopathology (Spearman's $\rho = 0.408$, $p < 0.001$), indicating that PVS on *ex vivo* MRI accurately reflects PVS enlargement on histopathology (Fig. 2). Importantly, *post-mortem* interval (*i.e.* the time between death and brain extraction) was not associated with average percentage of EPVS area on histopathology in our cohort (Spearman's $\rho = 0.365$, $p = 0.149$).

Consistent with the MRI findings, EPVS severity was significantly higher in the juxtacortical WM of CAA cases compared to the non-CAA cases on histopathology (Mann-Whitney U = 644.00, $p < 0.001$) (Fig. 2). No significant difference was detected in the BG on histopathology between groups (Mann-Whitney U = 47.00, $p = 0.999$) (Supplementary Fig. 1).

EPVS burden is positively associated with CAA severity

Next, we assessed the association between EPVS percentage area on histopathology and total CAA burden in overlying vessels, using LME models in the CAA cases only (n = 19 cases; n = 72 sections). Results are reported in Table 2. Of all the variables included in the models, total CAA percentage area and myelin rarefaction showed a significant positive effect on EPVS percentage area. The model with the overall best fit included both total CAA percentage area (i.e. cortical and leptomeningeal CAA combined) and myelin rarefaction (comparison between null model (0) and (3a): χ^2 (2) = 14.89, $p < 0.001$) and explained 52% of the variance of the EPVS. Conversely, percentage area of fibrin positive blood vessels in the WM (as a measure of BBB-leakage) and percentage area of cortical Aβ-plaques (as a measure of AD pathology) had no significant effect on total CAA (Fig.3). Furthermore, corresponding LME models that differentiated between leptomeningeal and cortical CAA were also implemented. In these models, which explained less variance than those that considered total CAA, only leptomeningeal CAA and not cortical CAA had a significant effect (Supplementary Table 1). Collectively, these findings suggest that the accumulation of vascular Aβ in the walls of cortical and leptomeningeal blood vessels, rather than Aβ plaques or BBB leakage is associated with PVS enlargement in the underlying WM and that this effect is driven by leptomeningeal CAA.

PVS enlarge around the WM portion of perforating cortical arteries affected by CAA

The in-depth characterization of the morphology of MRI-visible PVS and the PVS-related vessels was performed on the ultra-high resolution (100 μm isotropic) T2-weighted sequence of samples from cases no. 5 and 13 (Fig. 4 and Supplementary Videos 1 and 2). The increased spatial resolution allowed tracing individual PVS and PVS-related vessels at much greater detail compared to whole hemisphere *ex vivo* 3 tesla MRI and clinical *in vivo* MRI. Two key observations were made: 1) EPVS in the juxtacortical WM were found surrounding individual blood vessels that originate from the pial surface (i.e. cortical perforating vessels). (Fig. 5 and Supplementary Videos 1 and 2); 2) Some of the EPVS, especially in the case with more severely enlarged PVS, continued into the cortex (Supplementary Fig. 5 and 6). Using deep learning-derived segmentations, the number of EPVS in the WM and GM was detected (EPVS in the GM/EPVS in the WM: case no. 5 = 26/1229 (2.1%); case no. 13 = 378/910 (41.5%)). These observations were confirmed in the histopathological serial sections (Fig. 5).

In the single-vessel analysis, a total of n = 284 individual vessels were identified in the WM on 8 H&E-stained sections. Four needed to be excluded from the analysis because the same vessel could not be found on the adjacent SMA-stained section. The frequency of EPVS in the analyzed serial sections of sample no. 13 (case with severe MRI-visible PVS) was higher than in sample no. 5 (case with mild MRI-visible PVS) (31/102 (30%) vs. 137/182 (75%); $\chi^2(1) = 54.77$; n = 280, $p < 0.001$). Notably, we did not find any EPVS on histopathology without a central blood vessel. When assessing the adjacent SMA-stained sections, we found that 147/167 (88%) of the EPVS-related vessels were arterioles and 20/167 (12%) were venules ($\chi^2(1) = 28.29$; n = 280, $p < 0.001$) (Fig. 5). This observation suggests that primarily spaces surrounding arterioles rather than venules become enlarged. Interestingly, we noticed Aβ-positivity in the juxtacortical WM portion of the walls of several vessels. This was significantly more likely in vessels with EPVS than in those without ($\chi^2(1) = 4.15$; n=280, $p = 0.042$), suggesting that PVS enlarge mainly around CAA-laden vessels. Moreover, vessels positive for Aβ in the WM showed extensive loss of SMA and excessive Aβ deposition in the cortical segment of the same vessels. Extending this observation to all CAA cases, a significant positive correlation between the percentage area of CAA in the WM, calculated using the AI Aβ model as WM CAA area [mm^2]/WM tissue area [mm^2], and percentage area of EPVS on histopathology was found (n = 72; Spearman's $\rho = 0.258$; $p = 0.029$) (Fig. 5). PVS enlargement is thus associated with the presence of CAA in the WM portion of individual arterioles and suggests that impaired clearance of Aβ along CAA-affected cortical arterioles results in the accumulation of fluid and Aβ depositions in the WM portion of the same arterioles.

EPVS in hereditary CAA are comparable to EPVS in sporadic CAA

The observations made in the two tissue blocks derived from the sporadic CAA cases, were confirmed in the D-CAA case: 1) EPVS in the juxtacortical WM surrounded individual blood vessels that originated from the pial surface (i.e. cortical perforating vessels) (Supplementary Fig. 4 and Supplementary Video 4); 2) The deep-learning derived segmentations showed that part of the EPVS extended into the cortex (EPVS in the GM/EPVS in the WM = 174/662) (Supplementary Fig. 7); 3) In the single-vessel analysis on the serial sections, a total of n = 261 individual vessels were identified in the WM on 4 H&E-stained sections. One needed to be excluded from the analysis since the same vessel could not be found on the adjacent SMA-stained section. 215 vessels were related to an EPVS, whereas 46 were not. On adjacent SMA-stained sections, we found that 190/215 (88.37%) of the EPVS-related vessels were arterioles compared to 27/46 (59%) of the non-EPVS-related vessels ($\chi^2(1) = 23.44$; n = 261, $p < 0.001$) (Supplementary Fig. 4). Few vessels were positive for Aβ in the WM: 2/46 were not related to an EPVS, 4/215 were ($\chi^2(1) = 0.92$; n = 261, $p = 0.336$). Overall, these observations are comparable to those in the sporadic CAA cases.

Discussion

The results of the present study indicate that in CAA PVS enlarge predominantly around the WM portion of perforating cortical arterioles. We also found that EPVS burden in brains with CAA is locally associated with CAA severity of the overlying portions of the same vessels and with presence of CAA in the WM, independent of other related pathological markers. These results support the notion of outward flow alongside the walls of cortical arterioles and suggest that impaired perivascular clearance of Aβ might lead to fluid stagnation and thus enlargement of the PVS around the upstream portion of connected perivascular compartments.

Our results are in line with previous studies that found an association between MRI-visible PVS score and CAA severity on histopathology [64] and Aβ deposition measured with positron emission tomography during life [17, 51]. Considering that PVS enlargement likely reflects impaired perivascular clearance [1, 43, 69], vascular accumulation of Aβ has been proposed as part of a self-reinforcing mechanism, that leads to a clearance block [27] and thus enlargement of the PVS [41]. Experimental evidence supports the notion that CAA may be the result of impaired Aβ clearance along the cerebral vessels. Animal studies have reported that tracer injected in the brain accumulates in the walls of cerebral vessels, reproducing the pattern of human CAA [14]. Furthermore, perivascular drainage of tracer is impaired in the ageing mouse brain in the presence of vascular Aβ [27]. In human brains with AD pathology, which very frequently exhibit co-existing CAA [37], removal of Aβ plaques achieved by experimental active anti-Aβ immunotherapy was associated with worsening of cortical and leptomeningeal CAA [9], suggesting, that once dislocated from the plaques, Aβ is cleared along the cerebral vessels.

The observations made in this study address existing assumptions on EPVS of the human brain [69], and thus allow us to make more data-driven suggestions regarding clearance pathways. Firstly, the results build a clear bridge from the MRI-visible PVS detected with *in vivo* MRI, to those detected on *ex vivo* imaging, and ultimately to the EPVS observed on histopathology. These results add to previous studies, that have also sought to pinpoint the histopathological correlates of MRI-visible PVS of *ex vivo* MRI [34, 61] and to define EPVS in histopathology [54, 72], showing that EPVS are distinguishable from artefacts due to formalin fixation. Even though the severity in grade was comparable, the width of MRI-visible PVS on *in vivo* MRI differed from the width of MRI-visible PVS on *ex vivo* MRI, as measured in two representative cases. This is to be expected and could reflect changes induced by formalin fixation, or differences in spatial resolution, where PVS may appear larger on *in vivo* MRI due to partial volume effects. Furthermore, the increased numbers of EPVS in the CSO or juxtacortical WM compared to the BG, both on *ex vivo* MRI and histopathology, confirmed previous reports in patients with CAA [18, 19]. The observation of greater severity of PVS in the BG on *ex vivo* compared to *in vivo* MRI could reflect previous reports that PVS become more visible with increasing age, especially in the BG [24, 75].

Secondly, we found that the spaces enlarge primarily around cortical perforating vessels that continue into the WM. In fact, as shown in human anatomical studies, cortical medullary arteries dive in the cortex and continue into the WM of the CSO [62]. Ultra-high resolution 7 tesla MRI (with its small voxel size of 100 μm isotropic and high signal-to-noise ratio) provided the necessary level of detail to depict both the MRI-visible PVS and their related vessels, which were found to originate from the cortex extending into the WM. Cortical vessels were often affected by CAA in the cortex of the CAA cases.

Third, the quantification performed on the serial sections showed that the vast majority of the vessels related to EPVS are arterioles. This is consistent with previous observations obtained from *in vivo* 7 tesla MRI, which indicated MRI-visible PVS around arterioles, but not venules [10]. Similarly, a lack of overlap between MRI-visible PVS and venules in the CSO was observed in a larger cohort of patients with CSVD [35]. Fourth, presence of Aβ was also observed in the WM portion of the same perforating vessels, decreasing in intensity with increasing distance from the cortex. This pattern could emerge due to a blockage of Aβ clearance towards the brain surface, which resembles decreasing severity of CAA between superficial and deep cortical layers, as previously shown [37]. Consistent with this explanation, not only total CAA percentage area, but also WM CAA percentage area were associated with EPVS burden.

Collectively, our results suggest outward perivascular Aβ clearance along the cerebral arteries in the opposite direction of blood flow (see. Fig. 6 for schematic reference), as previously suggested [13]. The exact mechanisms behind peri-arteriolar clearance still need to be elucidated. It has been suggested that spontaneous vasomotion, generated by the slow contractions and dilations of smooth muscle cells, may be a possible driving force [28], which in animal [65] and mathematical models [2, 22], has also been shown to correlate with clearance rates. Notably, vasomotion is reduced in mice with CAA and may be related to the loss of function of smooth muscle cells [65]. While our observations lend support to this paradigm, they do not exclude other possible clearance mechanisms and pathways [1, 7]. In particular, Aβ deposition in cortical arterioles could possibly reflect a local perturbation of Aβ movement in the context of reduced inward flow along arterioles in the pathophysiology of the disease, as proposed by the glymphatic system [8]. Additional experiments in the living brain as well as computational modeling are warranted to test both hypotheses.

Findings in sporadic CAA cases were consistent with observations in tissue from the hereditary D-CAA case [42], indicating that our conclusions may be generalizable to this genetic disease, caused exclusively by production of E22Q Aβ, a form of Aβ that is less soluble than wild-type Aβ [40]. The inclusion of hereditary CAA in this study is valuable, because it suggests that in this “pure” form of CAA (in the absence of age-related vascular risk factors), clearance dysfunction may also be an important piece of the pathophysiological process. MRI-visible PVS can be observed in several illnesses, including other forms of CSVD, such as hypertensive arteriopathy [60] and CADASIL [74]. Understanding whether in these conditions PVS enlargement follows similar patterns as described here requires dedicated studies. Generally, deepening the knowledge on the dynamics of clearance and why it fails with age and neurodegenerative disease is central to identifying therapies that promote the clearance of Aβ in the prevention and treatment of AD and CAA.

The mechanisms leading to the enlargement of PVS likely involve factors other than clearance impairment due to Aβ accumulation in the walls of cortical arterioles. For example, myelin rarefaction in the WM was here strongly associated with EPVS percentage area. A link between PVS enlargement and inflammation-triggered demyelination has been hypothesized [12], but lower myelin density could also reflect a lower tissue density, that thus more easily gives in to the accumulation of fluid in the PVS. On the other hand, our measure of density is based on the intensity of the WM (after masking EPVS), which could also decrease due to fluid accumulation within the extracellular tissue (interstitial edema), possibly as a consequence of impaired clearance [39]. Abnormalities of the vessel wall independent from CAA, such as arteriolosclerosis, have been associated with PVS enlargement in pathological analyses [12, 26]. It is therefore plausible that dysfunction of the vessel wall, regardless of the pathology that causes it, can lead to perivascular clearance impairment. However, the relationship between inflammatory activity and severity of MRI-visible PVS in systemic lupus erythematosus [45] and multiple sclerosis [73], suggests that other factors, such as neuroinflammation and BBB-leakage, might also play a role in EPVS formation. In our study cohort, no evidence of an association between BBB-leakage, measured by fibrin accumulation in the vessel wall, and EPVS was found. Future analyses that take into account arteriolosclerosis, presence of neuroinflammatory cells in proximity of the EPVS, and that differentiate between types of Aβ-plaques and capillary CAA, could provide further insight into the mechanisms of PVS enlargement.

Limitations of this study include the small sample size and the cross-sectional nature of histopathological analyses, which prevents us from determining the sequence of events leading to the enlargement of PVS in the presence of CAA. Moreover, due to the heterogeneity of the *in vivo* MRI scans, we were not able to reliably perform deep learning-based automatic segmentations to determine the burden of MRI-visible PVS *in vivo* [23, 29, 59]. Instead, we relied on semiquantitative scores for the quantification of PVS on *in vivo* and 3 tesla *ex vivo* MRI, which is less desirable, but ensures the adequate comparison between *ante-* and *post-mortem* scans. Finally, this cohort represents a highly selective group of individuals that participated in brain donation, as such it remains unclear how these findings generalize to the larger aging population.

To conclude, we found that in human brains with a pathologically confirmed clinical diagnosis of sporadic CAA, burden of MRI-visible PVS *in vivo* reflects EPVS severity on histopathology. By incorporating single-vessel analyses, this study further adds to the literature by providing more direct evidence of the association between presence of cortical CAA and enlargement of PVS in the underlying WM. In fact, relying on ultra-high resolution *ex vivo* MRI, deep learning-based quantification of pathological markers and serial sectioning, we found that EPVS are located mainly around the WM portion of perforating cortical arterioles, and not venules, and that their burden is associated with CAA severity. Collectively, these findings are consistent with the notion of outward peri-arterial drainage and with a self-reinforcing process including loss of smooth muscle cells and vessel function, that might lead to clearance impairment of vascular Aβ and enlargement of the PVS around connected perivascular compartments of the same vessel. A better understanding of these mechanisms is crucial to design therapies able to reduce Aβ accumulation in CAA and AD. Studies that include a greater number of cases and other pathologies are needed, to establish whether similar associations apply to ageing and other neurodegenerative diseases.

Supplementary Material

Refer to Web version on PubMed Central for supplementary material.

Acknowledgments

We wish to thank Sjoerd van Duinen, Gisela Terwindt, Marieke Wermer, and Louise van der Weerd from Leiden University Medical Center (LUMC) for providing the brain sample of the D-CAA case. Furthermore, we thank the patients and their families for participating in the brain donation program. This work was supported by the Harvard Catalyst, Harvard Clinical and Translational Science Center (National Center for Advancing Translational Sciences, National Institutes of Health Award UL1 TR002541). The content is solely the responsibility of the authors and does not necessarily represent the official views of Harvard Catalyst, Harvard University and its affiliated academic healthcare centers, or the National Institutes of Health.

Funding

This work was funded by the National Institutes of Health (AG059893 to S.J.v.V., RF1 NS110054 to B.J.B.; 1RF1MH123195-01 and 1R01AG070988-01 to J.E.I.), the German Research Foundation (DFG) (454245528 to V.P.), Alzheimer's Research UK (ARUK-IRG2019A-003), and the European Research Council (Starting Grant 677697, project "BUNGEE-TOOLS").

Data availability Statement

The data that support the findings of this study is available from the corresponding author upon reasonable request.

References:

1. Abbott NJ, Pizzo ME, Preston JE, Janigro D, Thorne RG (2018) The role of brain barriers in fluid movement in the CNS: is there a 'glymphatic' system? Acta Neuropathol 135:387–407. doi: 10.1007/s00401-018-1812-4 [PubMed: 29428972]
2. Aldea R, Weller RO, Wilcock DM, Carare RO, Richardson G (2019) Cerebrovascular smooth muscle cells as the drivers of intramural periarterial drainage of the brain. Front Aging Neurosci 11:1–17. doi: 10.3389/fnagi.2019.00001 [PubMed: 30740048]
3. Atzeni A, Jansen M, Ourselin S, Iglesias JE (2018) A probabilistic model combining deep learning and multi-atlas segmentation for semi-automated labelling of histology. Lect Notes Comput Sci 11071:219–227. doi: 10.1007/978-3-030-00934-2_25
4. Bacyinski A, Xu M, Wang W, Hu J (2017) The Paravascular Pathway for Brain Waste Clearance: Current Understanding, Significance and Controversy. Front Neuroanat 11:1–8. doi: 10.3389/fnana.2017.00101 [PubMed: 28144216]
5. Banerjee G, Kim HJ, Fox Z, Jäger HR, Wilson D, Charidimou A, Na HK, Na DL, Seo SW, Werring DJ (2017) MRI-visible perivascular space location is associated with Alzheimer's disease independently of amyloid burden. Brain 140:1107–1116. doi: 10.1093/brain/awx003 [PubMed: 28335021]
6. Bates D, Mächler M, Bolker BM, Walker SC (2015) Fitting linear mixed-effects models using lme4. J Stat Softw 67. doi: 10.18637/jss.v067.i01

7. Benveniste H, Liu X, Koundal S, Sanggaard S, Lee H, Wardlaw J (2019) The Glymphatic System and Waste Clearance with Brain Aging: A Review. Gerontology 65:106–119. doi: 10.1159/000490349 [PubMed: 29996134]
8. Benveniste H, Nedergaard M (2022) Cerebral small vessel disease: A glymphopathy? Curr Opin Neurobiol 72:15–21. doi: 10.1016/j.conb.2021.07.006 [PubMed: 34407477]
9. Boche D, Zotova E, Weller RO, Love S, Neal JW, Pickering RM, Wilkinson D, Holmes C, Nicoll JAR (2008) Consequence of Aβ immunization on the vasculature of human Alzheimer's disease brain. Brain 131:3299–3310. doi: 10.1093/brain/awn261 [PubMed: 18953056]
10. Bouvy WH, Biessels GJ, Kuijf HJ, Kappelle LJ, Luijten PR, Zwanenburg JJM (2014) Visualization of perivascular spaces and perforating arteries with 7 T magnetic resonance imaging. Invest Radiol 49:307–313. doi: 10.1097/RLI.0000000000000027 [PubMed: 24473365]
11. Boyle PA, Yu L, Wilson RS, Leurgans SE, Schneider JA, Bennett DA (2018) Person-specific contribution of neuropathologies to cognitive loss in old age. Ann Neurol 83:74–83. doi: 10.1002/ana.25123 [PubMed: 29244218]
12. Brown R, Benveniste H, Black SE, Charpak S, Dichgans M, Joutel A, Nedergaard M, Smith KJ, Zlokovic BV, Wardlaw JM (2018) Understanding the role of the perivascular space in cerebral small vessel disease. Cardiovasc Res 114:1462–1473. doi: 10.1093/cvr/cvy113 [PubMed: 29726891]
13. Carare RO, Aldea R, Bulters D, Alzetani A, Birch AA, Richardson G, Weller RO (2020) Vasomotion Drives Periarterial Drainage of Aβ from the Brain. Neuron 105:400–401. doi: 10.1016/j.neuron.2020.01.011 [PubMed: 32027828]
14. Carare RO, Bernardes-Silva M, Newman TA, Page AM, Nicoll JAR, Perry VH, Weller RO (2008) Solutes, but not cells, drain from the brain parenchyma along basement membranes of capillaries and arteries: Significance for cerebral amyloid angiopathy and neuroimmunology. Neuropathol Appl Neurobiol 34:131–144. doi: 10.1111/j.1365-2990.2007.00926.x [PubMed: 18208483]
15. Charidimou A, Boulouis G, Gurol ME, Ayata C, Bacskai BJ, Frosch MP, Viswanathan A, Greenberg SM (2017) Emerging concepts in sporadic cerebral amyloid angiopathy. Brain 1–22. doi: 10.1093/brain/awx047 [PubMed: 28031214]
16. Charidimou A, Boulouis G, Pasi M, Auriel E, Van Etten ES, Haley K, Ayres A, Schwab KM, Martinez-Ramirez S, Goldstein JN, Rosand J, Viswanathan A, Greenberg SM, Gurol ME (2017) MRI-visible perivascular spaces in cerebral amyloid angiopathy and hypertensive arteriopathy. Neurology 88:1157–1164. doi: 10.1212/WNL.0000000000003746 [PubMed: 28228568]
17. Charidimou A, Hong YT, Jäger HR, Fox Z, Aigbirhio FI, Fryer TD, Menon DK, Warburton EA, Werring DJ, Baron JC (2015) White Matter Perivascular Spaces on Magnetic Resonance Imaging: Marker of Cerebrovascular Amyloid Burden? Stroke 46:1707–1709. doi: 10.1161/STROKEAHA.115.009090 [PubMed: 25908461]
18. Charidimou A, Jaunmuktane Z, Baron JC, Burnell M, Varlet P, Peeters A, Xuereb J, Jäger R, Brandner S, Werring DJ (2014) White matter perivascular spaces: An MRI marker in pathology-proven cerebral amyloid angiopathy? Neurology 82:57–62. doi: 10.1212/01.wnl.0000438225.02729.04 [PubMed: 24285616]
19. Charidimou A, Meegahage R, Fox Z, Peeters A, Vandermeeren Y, Laloux P, Baron JC, Jäger HR, Werring DJ (2013) Enlarged perivascular spaces as a marker of underlying arteriopathy in intracerebral haemorrhage: A multicentre MRI cohort study. J Neurol Neurosurg Psychiatry 84:624–629. doi: 10.1136/jnnp-2012-304434 [PubMed: 23412074]
20. Çiçek Ö, Abdulkadir A, Lienkamp SS, Brox T, Ronneberger O (2016) 3D U-net: Learning Dense Volumetric Segmentation from Sparse Annotation. arXiv:160606650v1 [csCV]. doi: 10.1007/978-3-319-46723-8_49
21. Clevert DA, Unterthiner T, Hochreiter S (2016) Fast and Accurate Deep Network Learning by Exponential Linear Units (ELUs). arXiv:151107289v5 [csLG]
22. Diem AK, Sharp MMG, Gatherer M, Bressloff NW, Carare RO, Richardson G (2017) Arterial pulsations cannot drive intramural periarterial drainage: Significance for Aβ drainage. Front Neurosci 11:1–9. doi: 10.3389/fnins.2017.00475 [PubMed: 28154520]

23. Dubost F, Yilmaz P, Adams H, Bortsova G, Ikram MA, Niessen W, Vernooij M, de Bruijne M (2019) Enlarged perivascular spaces in brain MRI: Automated quantification in four regions. Neuroimage 185:534–544. doi: 10.1016/j.neuroimage.2018.10.026 [PubMed: 30326293]
24. Francis F, Ballerini L, Wardlaw JM (2018) Perivascular spaces and their associations with risk factors, clinical disorders and neuroimaging features: A systematic review and meta-analysis. Int J Stroke 14:359–371. doi: 10.1177/1747493019830321
25. Greenberg SM, Bacskai BJ, Hernandez-Guillamon M, Pruzin J, Sperling R, van Veluw SJ (2020) Cerebral amyloid angiopathy and Alzheimer disease — one peptide, two pathways. Nat Rev Neurol 16:30–42. doi: 10.1038/s41582-019-0281-2 [PubMed: 31827267]
26. Grinberg LT, Thal DR (2010) Vascular pathology in the aged human brain. Acta Neuropathol 119:277–290. doi: 10.1007/s00401-010-0652-7 [PubMed: 20155424]
27. Hawkes CA, Härtig W, Kacza J, Schliebs R, Weller RO, Nicoll JA, Carare RO (2011) Perivascular drainage of solutes is impaired in the ageing mouse brain and in the presence of cerebral amyloid angiopathy. Acta Neuropathol 121:431–443. doi: 10.1007/s00401-011-0801-7 [PubMed: 21259015]
28. Hawkes CA, Jayakody N, Johnston DA, Bechmann I, Carare RO (2014) Failure of perivascular drainage of β-amyloid in cerebral amyloid angiopathy. Brain Pathol 24:396–403. doi: 10.1111/bpa.12159 [PubMed: 24946077]
29. Hou Y, Park SH, Wang Q, Zhang J, Zong X, Lin W, Shen D (2017) Enhancement of Perivascular Spaces in 7 T MR Image using Haar Transform of Non-local Cubes and Block-matching Filtering. Sci Rep 7:1–12. doi: 10.1038/s41598-017-09336-5 [PubMed: 28127051]
30. Iglesias JE, Sabuncu MR (2015) Multi-atlas segmentation of biomedical images: A survey. Med Image Anal 24:205–219. doi: 10.1016/j.media.2015.06.012 [PubMed: 26201875]
31. Iliff JJ, Nedergaard M, Lee H, Yu M, Benveniste H, Feng T, Logan J (2013) Brain-wide pathway for waste clearance captured by contrast-enhanced MRI. J Clin Invest 123(3):1299–1309. doi: 10.1172/JCI67677 [PubMed: 23434588]
32. Iturria-Medina Y, Sotero RC, Toussaint PJ, Mateos-Pérez JM, Evans AC, Weiner MW, et al. (2016) Early role of vascular dysregulation on late-onset Alzheimer's disease based on multifactorial data-driven analysis. Nat Commun 7:11934. doi: 10.1038/ncomms11934 [PubMed: 27327500]
33. Jäkel L, De Kort AM, Klijn CJM, Schreuder FHBM, Verbeek MM (2021) Prevalence of cerebral amyloid angiopathy: A systematic review and meta-analysis. Alzheimer's Dement 1–19. doi: 10.1002/alz.12366
34. Javierre-Petit C, Schneider JA, Kapasi A, Makkinejad N, Tamhane AA, Leurgans SE, Mehta RI, Barnes LL, Bennett DA, Arfanakis K (2020) Neuropathologic and Cognitive Correlates of Enlarged Perivascular Spaces in a Community-Based Cohort of Older Adults. Stroke 51:2825–2833. doi: 10.1161/STROKEAHA.120.029388 [PubMed: 32757750]
35. Jochems ACC, Blair GW, Stringer MS, Thrippleton MJ, Clancy U, Chappell FM, et al. (2020) Relationship between Venules and Perivascular Spaces in Sporadic Small Vessel Diseases. Stroke 51:1503–1506. doi: 10.1161/STROKEAHA.120.029163 [PubMed: 32264759]
36. Kiviniemi V, Wang X, Korhonen V, Keinänen T, Tuovinen T, Autio J, Levan P, Keilholz S, Zang YF, Hennig J, Nedergaard M (2016) Ultra-fast magnetic resonance encephalography of physiological brain activity-Glymphatic pulsation mechanisms? J Cereb Blood Flow Metab 36(6):1033–1045. doi: 10.1177/0271678X15622047 [PubMed: 26690495]
37. Kövari E, Herrmann FR, Gold G, Hof PR, Charidimou A (2017) Association of cortical microinfarcts and cerebral small vessel pathology in the ageing brain. Neuropathol Appl Neurobiol 43:505–513. doi: 10.1111/nan.12366 [PubMed: 27783888]
38. Kress BT, Iliff JJ, Xia M, Wang M, Wei H et al. (2014) Impairment of paravascular clearance pathways in the aging brain. Ann Neurol 76:845–861. doi: 10.1002/ana.24271.Impairment [PubMed: 25204284]
39. Lei Y, Han H, Yuan F, Javeed A, Zhao Y (2017) The brain interstitial system: Anatomy, modeling, in vivo measurement, and applications. Prog Neurobiol 157:230–246. doi: 10.1016/j.pneurobio.2015.12.007 [PubMed: 26837044]

40. Maat-schieman M, Roos R, Van Duinen S (2005) Hereditary cerebral hemorrhage with amyloidosis- Dutch type. Neuropathology 25:288–297 10.1016/j.nbd.2003.08.019 [PubMed: 16382777]
41. MacGregor Sharp M, Bulters D, Brandner S, Holton J, Verma A, Werring DJ, Carare RO (2019) The fine anatomy of the perivascular compartment in the human brain:relevance to dilated perivascular spaces in cerebral amyloid angiopathy. Neuropathol Appl Neurobiol 45(3):305–308. doi: 10.1111/nan.12480 [PubMed: 29486067]
42. Martinez-Ramirez S, Van Rooden S, Charidimou A, Van Opstal AM, Wermer M, Edip Gurol M, Terwindt G, Van Der Grond J, Greenberg SM, Van Buchem M, Viswanathan A (2018) Perivascular spaces volume in sporadic and hereditary (Dutch-type) cerebral amyloid angiopathy. Stroke 49:1913–1919. doi: 10.1161/STROKEAHA.118.021137 [PubMed: 30012821]
43. Mestre H, Kostrikov S, Mehta RI, Nedergaard M (2017) Perivascular spaces, glymphatic dysfunction, and small vessel disease. Clin Sci 131(17):2257–2274. doi: 10.1042/cs20160381
44. Milletari F, Navab N, Ahmadi SA (2016) V-Net: Fully Convolutional Neural Networks for Volumetric Medical Image Segmentation. arXiv:160604797v1 [csCV]. doi: 10.1109/3DV.2016.79
45. Miyata M, Kakeda S, Iwata S, Nakayamada S, Ide S, Watanabe K, Moriya J, Tanaka Y, Korogi Y (2017) Enlarged perivascular spaces are associated with the disease activity in systemic lupus erythematosus. Sci Rep 7:1–10. doi: 10.1038/s41598-017-12966-4 [PubMed: 28127051]
46. Perosa V, Scherlek AA, Kozberg MG, Smith L, Bui TW, Auger CA, Vasylechko S, Greenberg SM, Van Veluw SJ (2021) Deep learning assisted quantitative assessment of histopathological markers of Alzheimer's disease and cerebral amyloid angiopathy. Acta Neuropathol Commun 9(1):141. doi: 10.1186/s40478-021-01235-1 [PubMed: 34419154]
47. Pollock H, Hutchings M, Weller RO, Zhang ET (1997) Perivascular spaces in the basal ganglia of the human brain: Their relationship to lacunes. J Anat 191:337–346. doi: 10.1017/S0021878297002458 [PubMed: 9418990]
48. Potter GM, Chappell FM, Morris Z, Wardlaw JM (2015) Cerebral Perivascular Spaces Visible on Magnetic Resonance Imaging: Development of a Qualitative Rating Scale and its Observer Reliability. Cerebrovasc Dis 39:224–231. doi: 10.1159/000375153 [PubMed: 25823458]
49. Power MC, Mormino E, Soldan A, James BD, Yu L, Armstrong NM, Bangen KJ, Delano-Wood L, Lamar M, Lim YY, Nudelman K, Zahodne L, Gross AL, Mungas D, Widaman KF, Schneider J (2018) Combined neuropathological pathways account for age-related risk of dementia. Ann Neurol 84:10–22. doi: 10.1002/ana.25246 [PubMed: 29944741]
50. Ellis RJ; Olichney JM; Thal LJ; Mirra SS; Morris JC; Beekly D; and Heyman A, Article (1996) Cerebral amyloid angiopathy in the brains of patients with Alzheimer's disease: The CERAD experience, part xv. Am Acad Neurol 46:1592–1596. doi: 10.1111/j.1532-5415.1997.tb00968.x
51. Raposo N, Planton M, Payoux P, Péran P, Albucher JF, Calviere L, Viguier A, Rousseau V, Hitzel A, Chollet F, Olivot JM, Bonneville F, Pariente J (2019) Enlarged perivascular spaces and florbetapir uptake in patients with intracerebral hemorrhage. Eur J Nucl Med Mol Imaging 46:2339–2347. doi: 10.1007/s00259-019-04441-1 [PubMed: 31359110]
52. Rasmussen MK, Mestre H, Nedergaard M (2018) The glymphatic pathway in neurological disorders. Lancet Neurol 17:1016–1024. doi: 10.1016/S1474-4422(18)30318-1 [PubMed: 30353860]
53. Reuter M, Rosas HD, Fischl B (2010) Highly accurate inverse consistent registration: A robust approach. Neuroimage 53:1181–1196. doi: 10.1016/j.neuroimage.2010.07.020 [PubMed: 20637289]
54. Roher AE, Kuo YM, Esh C, Knebel C, Weiss N, Kalback W, Luehrs DC, Childress JL, Beach TG, Weller RO, Kokjohn TA (2003) Cortical and leptomeningeal cerebrovascular amyloid and white matter pathology in Alzheimer's disease. Mol Med 9:112–122. doi: 10.1007/bf03402043 [PubMed: 12865947]
55. Rohlfing T, Brandt R, Menzel R, Maurer CR (2004) Evaluation of atlas selection strategies for atlas-based image segmentation with application to confocal microscopy images of bee brains. Neuroimage 21:1428–1442. doi: 10.1016/j.neuroimage.2003.11.010 [PubMed: 15050568]
56. Ronneberger O, Fischer Philipp, Brox T (2015) U-Net: Convolutional Networks for Biomedical Image Segmentation. arXiv:150504597 [csCV]. doi: 10.1109/ACCESS.2021.3053408

57. Satizabal CL, Zhu YC, Dufouil C, Tzourio C (2013) Inflammatory proteins and the severity of dilated Virchow-Robin spaces in the elderly. J Alzheimer's Dis 33:323–328. doi: 10.3233/JAD-2012-120874 [PubMed: 22976070]
58. Schindelin J, Arganda-Carrera I, Frise E, Verena K, Mark L, Tobias P, Stephan P, Curtis R, Stephan S, Benjamin S, Jean-Yves T, Daniel JW, Volker H, Kevin E, Pavel T, Albert C (2012) Fiji - an Open platform for biological image analysis. Nat Methods 9:676–682. doi: 10.1038/nmeth.2019.Fiji [PubMed: 22743772]
59. Sepehrband F, Barisano G, Sheikh-Bahaei N, Cabeen RP, Choupan J, Law M, Toga AW (2019) Image processing approaches to enhance perivascular space visibility and quantification using MRI. Sci Rep 9: 12351. doi: 10.1038/s41598-019-48910-x [PubMed: 31451792]
60. Shams S, Martola J, Charidimou A, Larvie M, Granberg T, Shams M, Kristoffersen-Wiberg M, Wahlund LO (2017) Topography and Determinants of Magnetic Resonance Imaging (MRI)-Visible Perivascular Spaces in a Large Memory Clinic Cohort. J Am Heart Assoc 6:1–8. doi: 10.1161/JAHA.117.006279
61. Swieten JCV, Den Hout JHWV, Ketel BAV, Hijdra A, Wokke JHJ, Van Gijn J (1991) Periventricular lesions in the white matter on magnetic resonance imaging in the elderly: A morphometric correlation with arteriolosclerosis and dilated perivascular spaces. Brain 114:761–774. doi: 10.1093/brain/114.2.761 [PubMed: 2043948]
62. Takahashi S (2010) Neurovascular Imaging, Springer-Verlag London limited.
63. Tarasoff-Conway JM, Carare RO, Osorio RS, Glodzik L, Butler T, Fieremans E, Axel L, Rusinek H, Nicholson C, Zlokovic BV, Frangione B, Blennow K, Ménard J, Zetterberg H, Wisniewski T, De Leon MJ (2015) Clearance systems in the brain - Implications for Alzheimer disease. Nat Rev Neurol 11(8):457–470. doi: 10.1038/nrneurol.2015.119 [PubMed: 26195256]
64. Van Veluw SJ, Biessels GJ, Bouvy WH, Spliet WGM, Zwanenburg JJM, Luijten PR, Macklin EA, Rozemuller AJM, Gurol ME, Greenberg SM, Viswanathan A, Martinez-Ramirez S (2016) Cerebral amyloid angiopathy severity is linked to dilation of juxtacortical perivascular spaces. J Cereb Blood Flow Metab 36(3):576–580. doi: 10.1177/0271678X15620434 [PubMed: 26661250]
65. van Veluw SJ, Hou SS, Calvo-Rodriguez M, Arbel-Ornath M, Snyder AC, Frosch MP, Greenberg SM, Bacskai BJ (2019) Vasomotion as a Driving Force for Paravascular Clearance in the Awake Mouse Brain. Neuron 105:549–561 doi: 10.1016/j.neuron.2019.10.033 [PubMed: 31810839]
66. van Veluw SJ, Scherlek AA, Freeze WM, ter Telgte A, van der Kouwe AJ, Bacskai BJ, Frosch MP, Greenberg SM (2019) Different microvascular alterations underlie microbleeds and microinfarcts. Ann Neurol. 86(2):279–292 doi: 10.1002/ana.25512 [PubMed: 31152566]
67. Venkat P, Chopp M, Zacharek A, Cui C, Zhang L, Li Q, Lu M, Zhang T, Liu A, Chen J (2017) White matter damage and glymphatic dysfunction in a model of vascular dementia in rats with no prior vascular pathologies. Neurobiol Aging 50:96–106. doi: 10.1016/j.neurobiolaging.2016.11.002 [PubMed: 27940353]
68. Wang M, Ding F, Deng S, Guo X, Wang W, Iliff JJ, Nedergaard M (2017) Focal Solute Trapping and Global Glymphatic Pathway Impairment in a Murine Model of Multiple Microinfarcts. J Neurosci 37:2870–2877. doi: 10.1523/jneurosci.2112-16.2017 [PubMed: 28188218]
69. Wardlaw JM, Benveniste H, Nedergaard M, Zlokovic BV, Mestre H, Lee H, Doubal FN, Brown R, Ramirez J, MacIntosh BJ, Tannenbaum A, Ballerini L, Rungta RL, Boido D, Sweeney M, Montagne A, Charpak S, Joutel A, Smith KJ, Black SE (2020) Perivascular spaces in the brain: anatomy, physiology and pathology. Nat Rev Neurol 16(3):137–153. doi: 10.1038/s41582-020-0312-z [PubMed: 32094487]
70. Wardlaw JM, Smith C, Dichgans M (2019) Small vessel disease: mechanisms and clinical implications. Lancet Neurol 18:684–696. doi: 10.1016/S1474-4422(19)30079-1 [PubMed: 31097385]
71. Webb AJS, Simoni M, Mazzucco S, Kuker W, Schulz U, Rothwell PM (2012) Increased cerebral arterial pulsatility in patients with leukoaraiosis: Arterial stiffness enhances transmission of aortic pulsatility. Stroke 43:2631–2636. doi: 10.1161/STROKEAHA.112.655837 [PubMed: 22923446]
72. Woollam DHM MJ (1968) Vascular tissues in the central nervous system. 486–498. in Pathology of the Nervous System; McGraw-Hill, New York.

73. Wuerfel J, Haertle M, Waiczies H, Tysiak E, Bechmann I, Wernecke KD, Zipp F, Paul F (2008) Perivascular spaces - MRI marker of inflammatory activity in the brain? Brain 131:2332–2340. doi: 10.1093/brain/awn171 [PubMed: 18676439]

74. Yao M, Hervé D, Jouvent E, Duering M, Reyes S, Godin O, Guichard JP, Dichgans M, Chabriat H (2014) Dilated Perivascular Spaces in Small-Vessel Disease: A Study in CADASIL. Cerebrovasc Dis 37:155–163. doi: 10.1159/000356982 [PubMed: 24503815]

75. Zhu YC, Tzourio C, Soumaré A, Mazoyer B, Dufouil C, Chabriat H (2010) Severity of dilated virchow-robin spaces is associated with age, blood pressure, and MRI markers of small vessel disease: A population-based study. Stroke 41:2483–2490. doi: 10.1161/STROKEAHA.110.591586 [PubMed: 20864661]

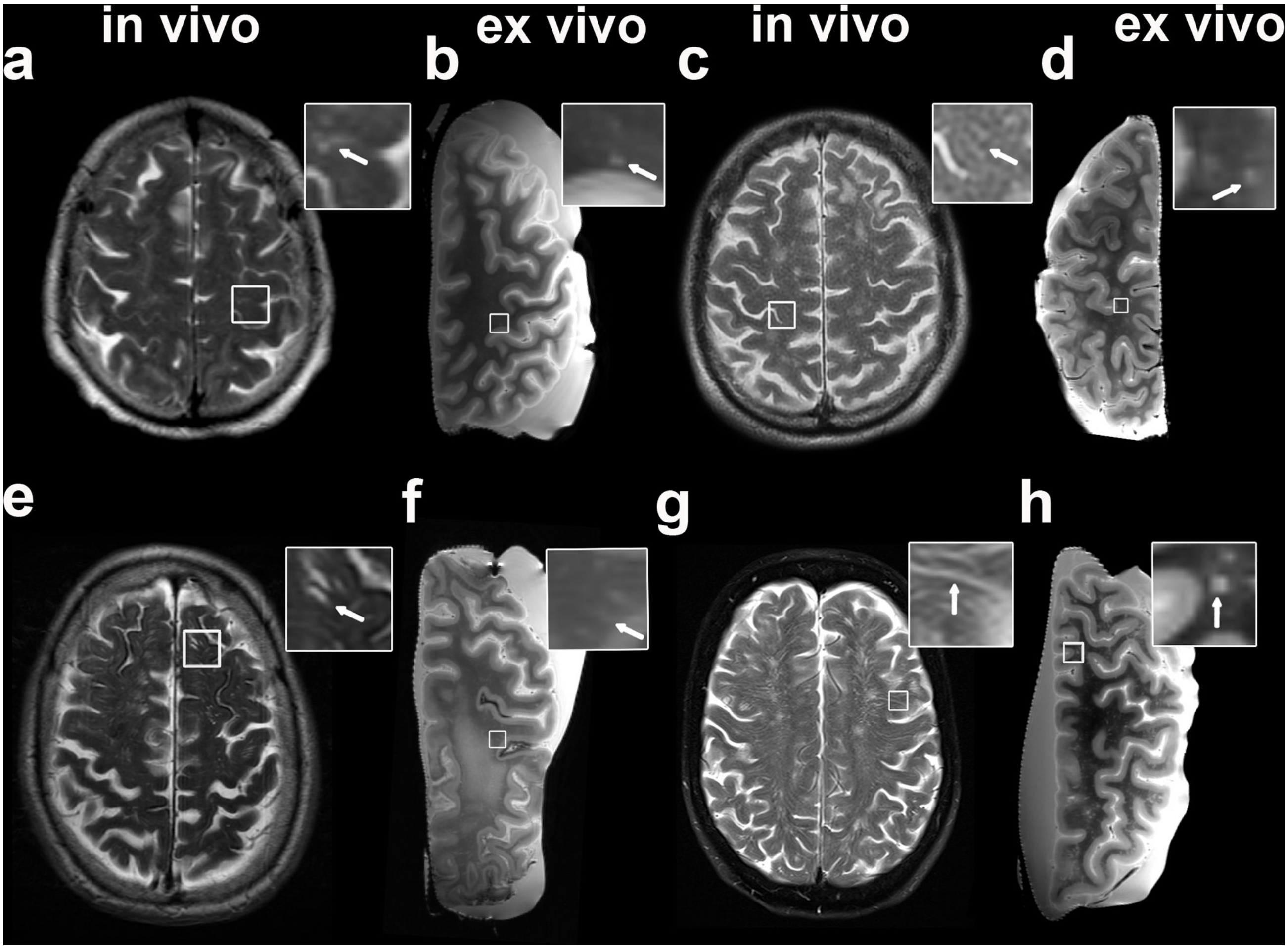

Fig. 1.

Examples of MRI-visible perivascular spaces (PVS) on in vivo and ex vivo MRI. The figure shows both examples of clinical in vivo (a, c, e, g) and of ex vivo (b, d, f, h) T2-weighted MRI scans of the same patient. The first is a case with mild degree of MRI-visible PVS in vivo and frequent after death (score in vivo 1 (a), ex vivo 3 (b); In vivo MRI-death interval: 7 months); the second case displays moderate MRI-visible PVS (score in vivo 2 (b), ex vivo 2 (c); In vivo MRI-death interval: 8 months). In the bottom row, a case with in vivo frequent and ex vivo severe (score in vivo 3 (e), ex vivo 4 (f); In vivo MRI-death interval: 53 months) and finally one with severe (score in vivo 4 (g), ex vivo 4 (h); In vivo MRI-death interval: 67 months) MRI-visible PVS are displayed. The insets show details of MRI-visible PVS (arrows)

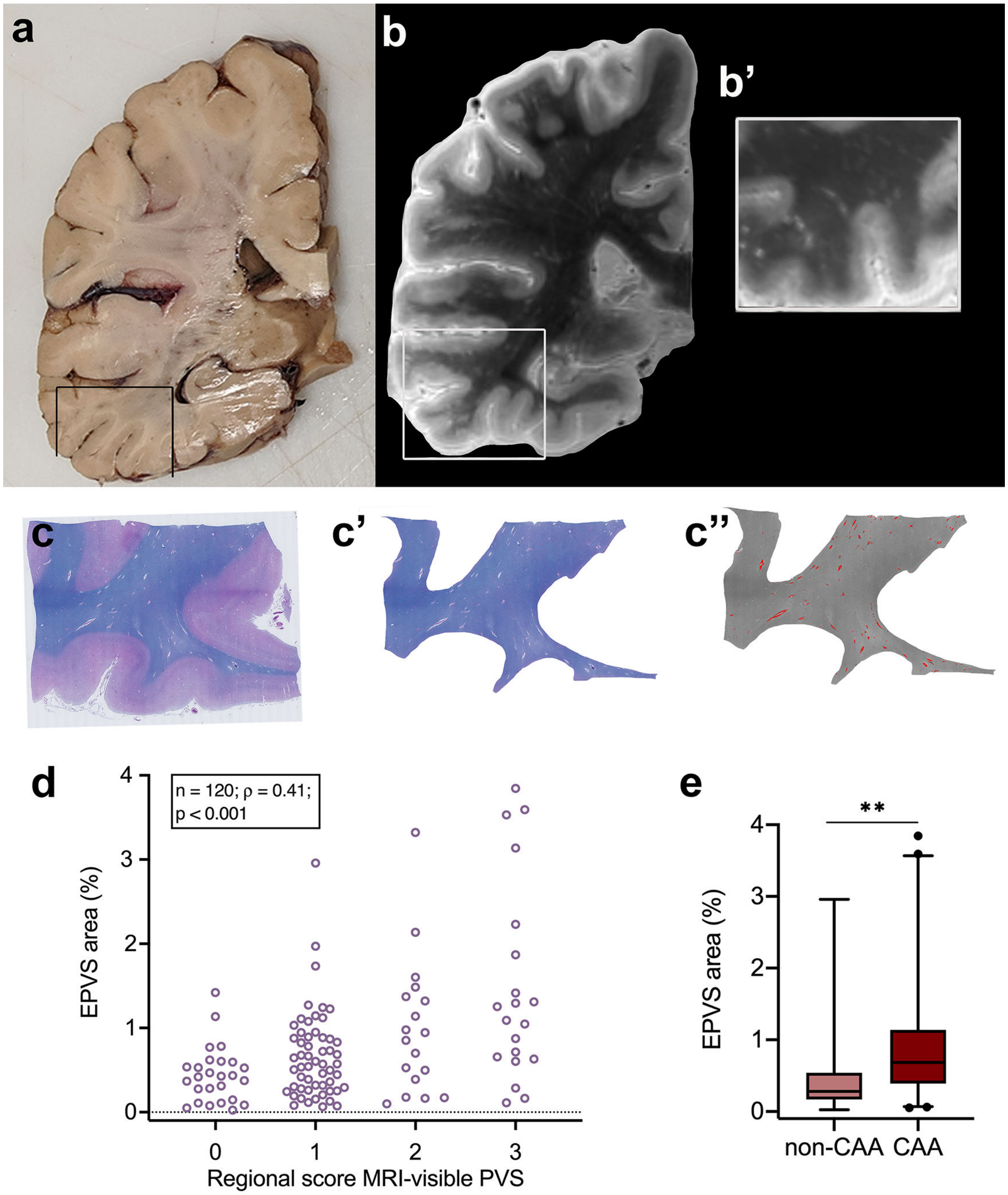

Fig. 2.

Quantification of enlarged perivascular spaces (EPVS) on ex vivo MRI and histopathology. Example of an approximately 1 cm thick coronally cut slab (a). The box highlights the region sampled for histopathology. Coronal view of the 3 tesla ex vivo turbo spin echo sequence of the same hemisphere at the corresponding level (b). The inset shows a higher magnification of the same area at the level assessed on histopathology for EPVS severity (b'). Luxol fast blue with Hematoxylin&Eosin (LHE)-stained section from the same sample (c), with corresponding manual segmentation of the white matter (c') and semi-automatic segmentation of the EPVS (overlaid in red) (c”). Positive correlation between the regional score of MRI-visible PVS and the percentage area of EPVS of the total white matter area, calculated on histopathological sections (one from the basal ganglia and four from cortical regions) of cases with and without CAA (d). EPVS percentage area in CAA cases was significantly higher than in non-CAA cases in the four cortical regions (frontal, temporal, parietal, and occipital). ** = $p < 0.01$ (e)

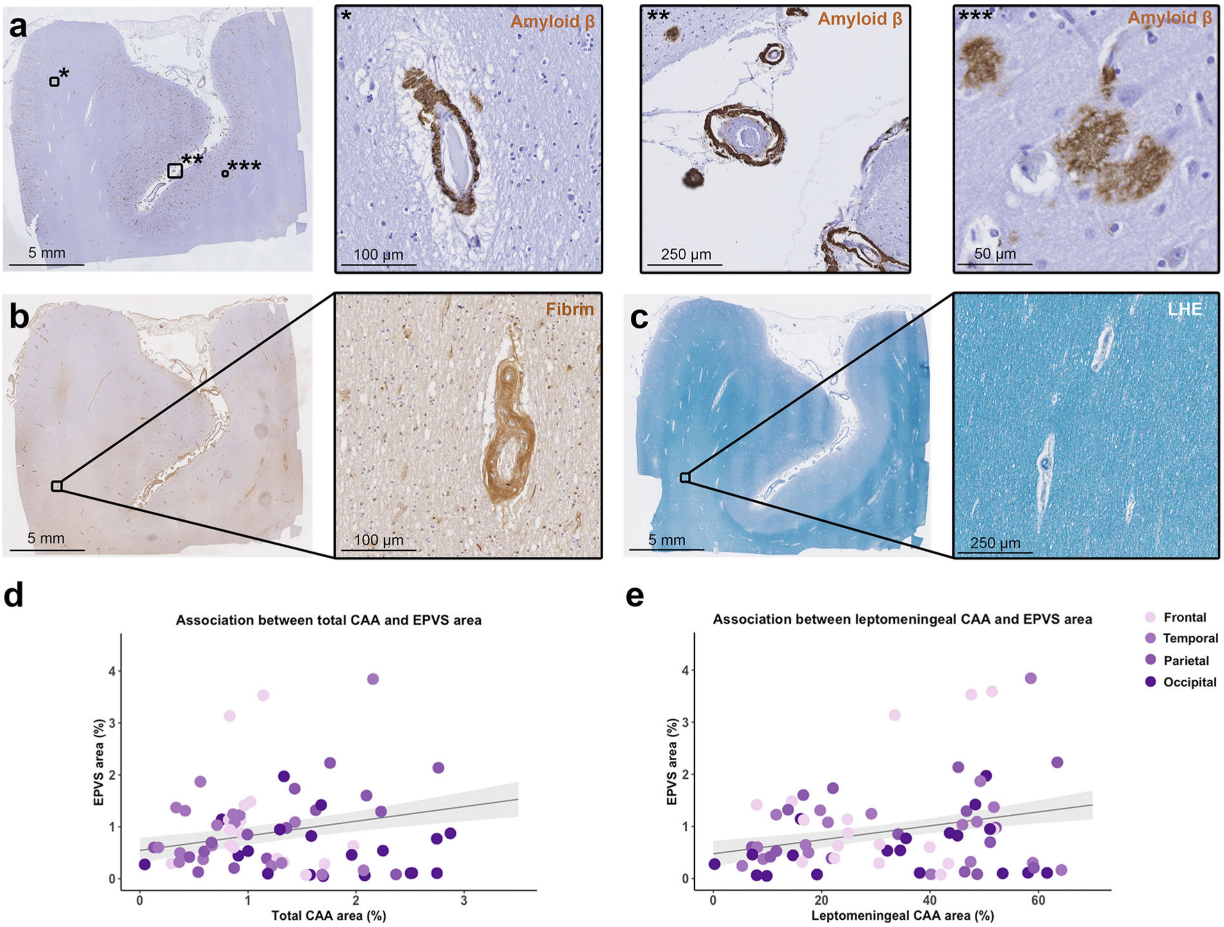

Fig. 3.

Correlation between enlarged perivascular spaces (EPVS) and cerebral amyloid angiopathy (CAA). The figure shows representative examples of the histopathological markers included in the analysis. Low magnification overview of a section that underwent immunohistochemistry against Aβ (a) and details of cortical CAA (*), leptomeningeal CAA (**) and Aβ plaques (***); an adjacent section that underwent immunohistochemistry against fibrin (b) and detail of a fibrin positive vessel in the white matter; a further adjacent section stained for Luxol fast blue with Hematoxylin&Eosin (LHE) (c) with detail of a portion of the white matter. Graphs representing the positive significant association between total CAA percentage area and EPVS percentage area in the cortical regions of CAA cases (d), and between leptomeningeal CAA percentage area and EPVS percentage area (e) (n = 19 cases; n = 72 sections; grey shadowed area shows the standard error of the model's prediction)

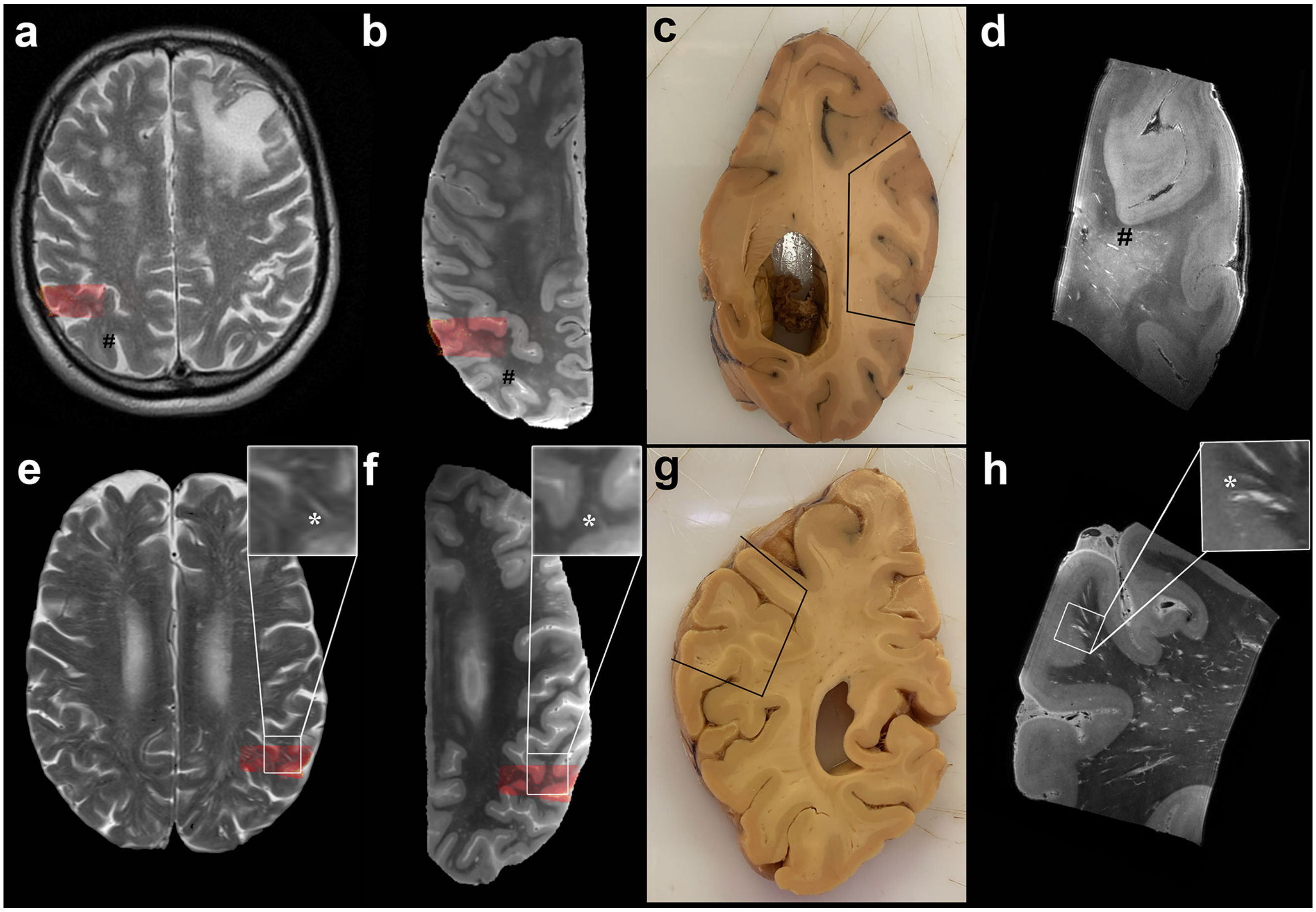

Fig. 4.

In depth characterization of MRI-visible perivascular spaces (PVS). Top row: MRI-visible PVS (mild degree) observed in the centrum semiovale on in vivo MRI of a case with neuropathologically confirmed CAA (case no. 5) (a). Corresponding ex vivo 3 tesla T2-weighted MRI scan of the right hemisphere, where some MRI-visible PVS are also observed (b) (indicated by #). Formalin fixed tissue of the same brain, on which the parietooccipital area sampled for ultra-high resolution ex vivo 7 tesla MRI is marked by the black line (c) and co-registered to in vivo and ex vivo 3 tesla MRI (red overlaid area). The enlarged PVS are clearly visible at the 100 μm isotropic resolution T2-weighted scan (#) (d). Bottom row: Evidence of severe degree of MRI-visible PVS on the T2-weighted in vivo MRI of case no. 13 (e), with corresponding ex vivo 3 tesla MRI of the left hemisphere (f), formalin fixed tissue (g) and ultra-high resolution T2-weighted scan (h). More MRI-visible PVS are observed in case no. 13 than case 5. The MRI-visible PVS appear to be confined to the WM on in vivo and ex vivo 3 tesla MRI, whereas they can be clearly seen to continue into the cortex at ultra-high resolution in this case (insets of the bottom row, *). The EPVS-related vessels are visible at 7 tesla as hypointense structures at the center of the EPVS. They originate at the pial surface as leptomeningeal vessels, dive into the cortex as cortical perforating vessels, and continue into the white matter (h). See also Supplementary Videos 1 - 3. For the purposes of registration between in vivo and ex vivo MRI the skull and the plastic bag in which the hemispheres were placed prior to scanning, were removed from the images

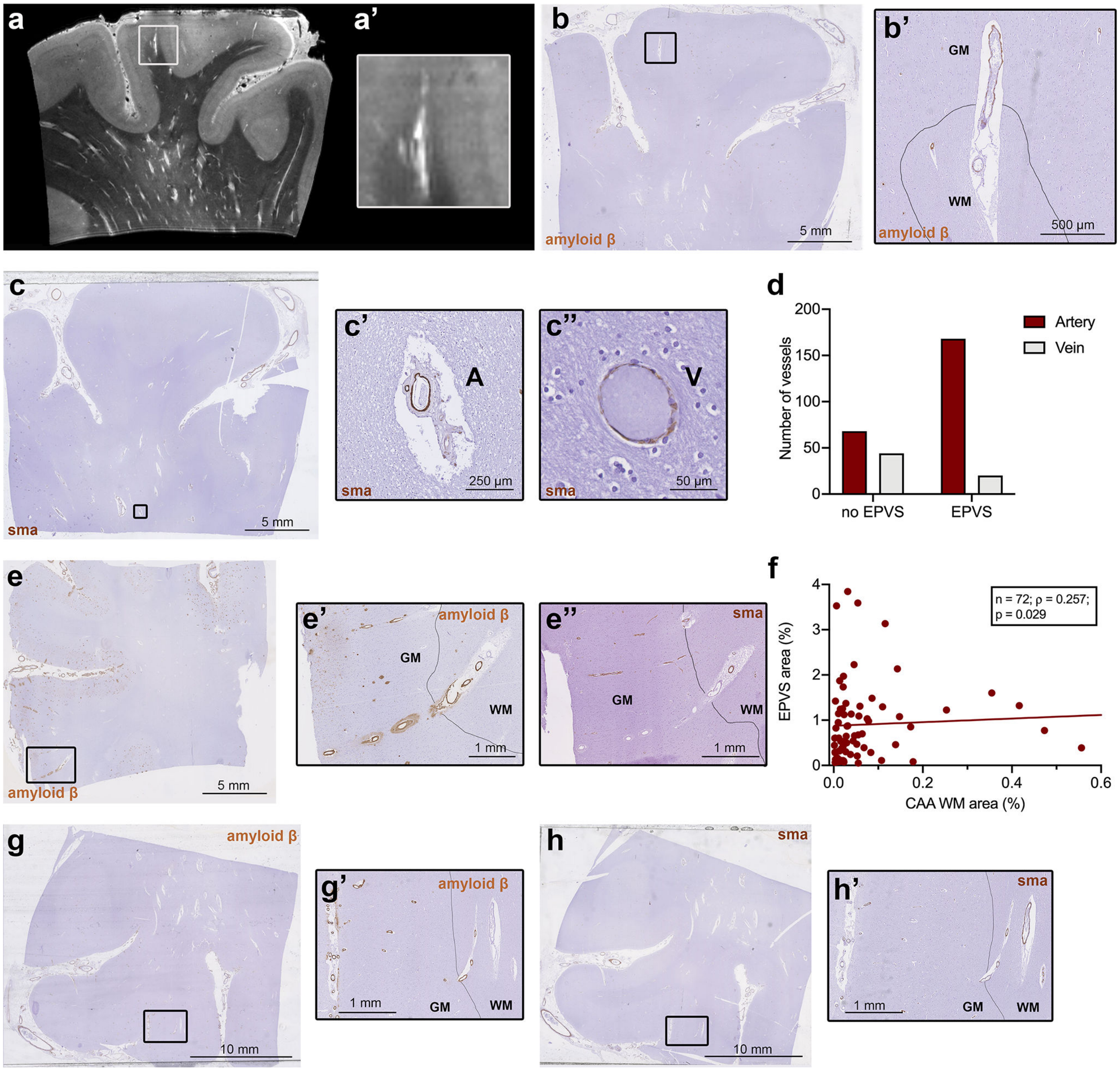

Fig. 5.

Histopathological characterization of individual blood vessels with surrounding enlarged perivascular spaces (EPVS). Ultra-high resolution 7 tesla turbo spin echo scan of case no. 13, with an example of an EPVS extending into the cortex (a, a’). The corresponding histopathological section, on which the drawn black line represents the boundary between grey matter (indicated by GM) and white matter (indicated by WM), confirms this observation (b, b’). On serial sections immunohistochemistry for smooth muscle actin (SMA) was performed (c) and revealed, that the vast majority of vessels with an EPVS were arterioles ($\chi^2(1) = 28.29$; n = 280; $p < 0.001$) (d), suggesting that EPVS are mainly peri-arteriolar (c’, A = artery) and not peri-venular (c”, V = vein). On some Aβ stained cortical sections, Aβ was present not only in the wall of the cortical portion of the vessel, but to a minor extent, also in the white matter portion of the same vessel (examples are b’, e’ and g’). The same vessels showed severe loss of SMA in the cortex, but not in the WM (e”, h’). A significant positive association was found between the percentage area of EPVS and the percentage area occupied by cerebral amyloid angiopathy (CAA) in the white matter, within all CAA cases (n=72 samples in 19 cases) (f)

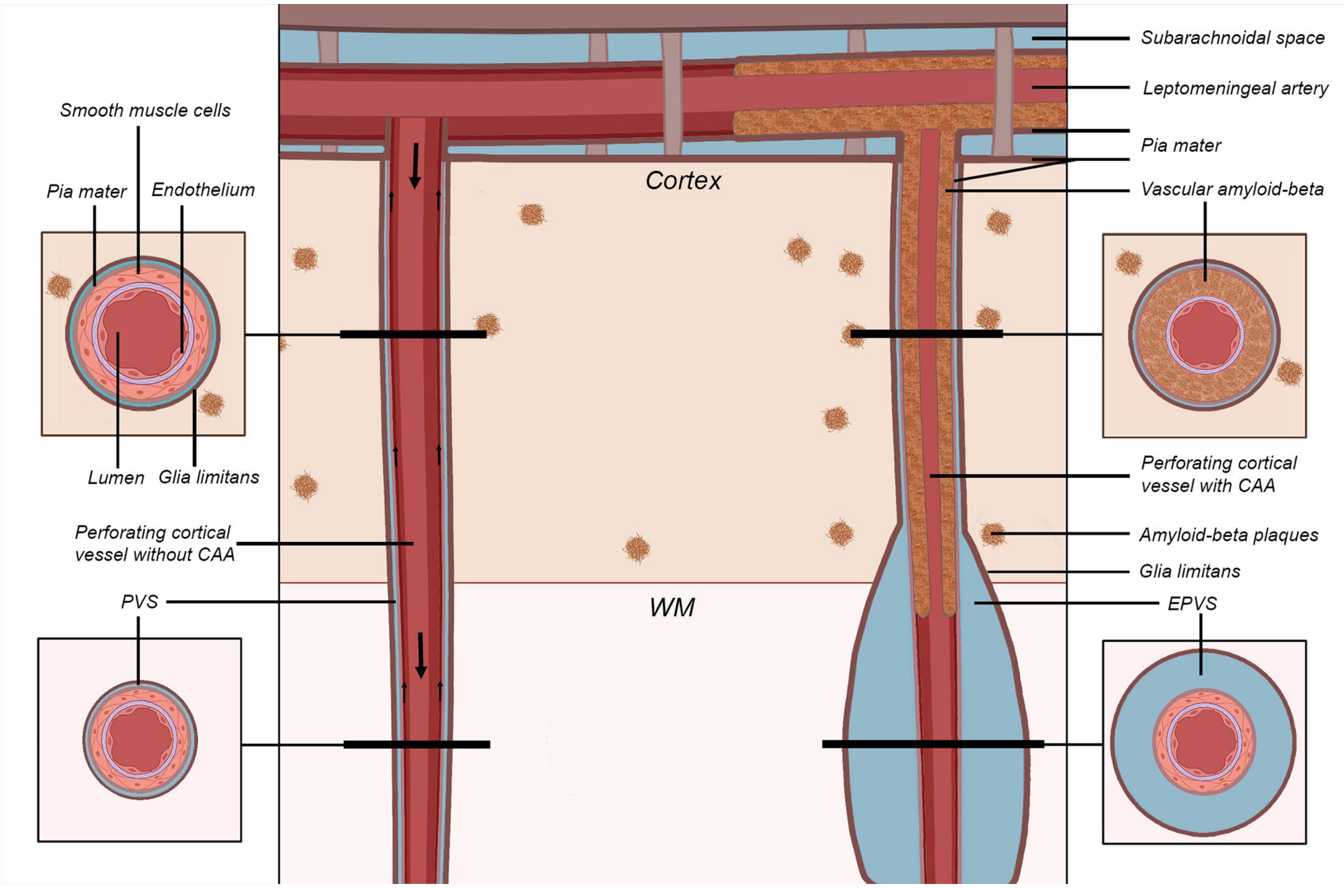

Fig. 6.

Schematic representation of the proposed mechanism of perivascular space (PVS) enlargement in cerebral amyloid angiopathy (CAA). The vessel on the left represents a healthy perforating artery (in red). The vessel on the right represents a perforating artery affected by CAA, in which Aβ accumulates within the tunica media of the wall of the cortical portion of the vessel (in brown), replacing the smooth muscle cells and leading to an enlargement of the PVS in the white matter portion of the same vessel (giving rise to the hypothesized self-reinforcing mechanism of continuing vascular Aβ accumulation). The smaller arrows on the left indicate the presumed direction of Aβ clearance along the vessel (either along the basement membranes or the perivascular compartment), while the bigger arrows represent the direction of blood flow. The results lend support to this proposed model of perivascular Aβ clearance. Key: CAA = cerebral amyloid angiopathy; EPVS = enlarged perivascular space; WM = white matter

Table 1:

Characteristics of the pathological cohort

Case No.	Path diagnosis	Age at death (years)	Sex	*In vivo* MRI-death interval (months)	*Post-mortem* interval (h)	MRI-visible PVS score (CSO) on *in vivo* MRI	MRI-visible PVS score (CSO) on ex *vivo* MRI	MRI-visible PVS score (BG) on *in vivo* MRI	MRI-visible PVS score (BG) on *ex vivo* MRI	Hypertension	Clinical presentation
1	CAA	80	M	16	N/A	3	4	0	1	Yes	Transient focal neurological episodes
2	CAA	70	M	N/A	16	N/A	4	N/A	0	Yes	ICH
3	CAA	76	M	17	27	4	4	1	1	No	ICH Cognitive Impairment
4	CAA	65	M	8	14	4	4	0	1	No	ICH
5	CAA	81	M	5	N/A	2	2	1	1	Yes	Transient focal neurological episodes
6	CAA	70	F	14	N/A	4	4	2	2	Yes	ICH
7	CAA	67	M	14	N/A	3	3	2	2	No	ICH
8	CAA	69	M	6	36	4	4	1	1	No	ICH
9	CAA	64	F	60	30	3	3	1	1	No	ICH Cognitive Impairment
10	CAA	79	F	55	37	3	4	3	2	Yes	ICH
11	CAA	67	M	18	24	3	4	1	1	Yes	ICH Transient focal neurological episodes
12	CAA	88	F	N/A	11	N/A	3	N/A	1	Yes	ICH
13	CAA	67	F	5	16	4	4	1	1	No	Transient focal neurological episodes Cognitive Impairment
14	CAA	84	F	53	32	2	4	1	2	Yes	N/A
15	CAA	67	M	78	N/A	2	2	1	1	Yes	ICH
16	CAA	76	M	157	20	3	4	0	1	No	ICH
17	CAA	78	F	47	24	N/A	2	N/A	1	N/A	ICH
18	CAA	86	M	53	20	3	4	2	3	Yes	Cognitive Impairment
19	CAA	85	M	66	N/A	0	2	0	3	Yes	ICH
1	No-CAA	90	M	47	N/A	N/A	2	N/A	2	No	No neurological diagnoses
2	No-CAA	95	F	70	4	1	2	0	2	Yes	TIA
3	No-CAA	88	F	17	9	3	4	1	4	Yes	Cognitive Impairment

Case No.	**Path diagnosis**	**Age at death (years)**	**Sex**	***In vivo* MRI-death interval (months)**	***Post-mortem* interval (h)**	**MRI-visible PVS score (CSO) on *in vivo* MRI**	**MRI-visible PVS score (CSO) on ex *vivo* MRI**	**MRI-visible PVS score (BG) on *in vivo* MRI**	**MRI-visible PVS score (BG) on *ex vivo* MRI**	**Hypertension**	**Clinical presentation**
4	No-CAA	85	M	7	38	1	3	2	1	Yes	Cognitive Impairment
5	No-CAA	82	F	25	N/A	3	3	2	2	Yes	Cognitive Impairment

Table 1 Characteristics of the pathological cohort. Key: M, male; F, female; CAA, cerebral amyloid angiopathy; CSO, centrum semiovale; BG, basal ganglia; N/A, not available; ICH, intracerebral hemorrhage; TIA, transient ischemic attack. Diagnoses of arterial hypertension during life and clinical phenotype were extracted from available medical records.

Table 2:

Associations between EPVS percentage area and total CAA

Models with total CAA						
	(0) Null model	**(1a) CAA only**	**(2a) With fibrin positive vessels (WM)**	**(3a) With myelin density**	**(4a) With cortical Aβ-plaques**	**(5a) Comprehensive model**
Age at death (y)	p = 0.388	p = 0.290	p = 0.287	p = 0.577	p = 0.284	p = 0.570
	−0.014 (−0.047 – 0.018)	−0.016 (−0.047 – 0.014)	−0.017 (−0.049–0.014)	−0.009 (−0.041– 0.023)	−0.016 (−0.047–0.014)	−0.009 (−0.041–0.022)
Sex	p = 0.896	p = 0.994	p = 0.925	p = 0.661	p = 0.848	p = 0.696
	−0.03418 (−0.564 – 0.502)	0.001 (−0.501 – 0.509)	0.025 (−0.503 – 0.594)	0.112 (−0.402–0.631)	−0.048 (−0.554–0.488)	0.106 (−0.431– 0.713)
CAA area (%)		**p = 0.037**	**p = 0.038**	**p = 0.014**	**p = 0.047**	**p = 0.016**
		0.280 (0.002 – 0.555)	0.291 (0.004 –0.582)	0.317 (0.060–0.571)	0.266 (−0.019– 0.544)	0.319 (0.048–0.591)
Fibrin positive vessels (WM) (%)			p = 0.797			p = 0.880
			−0.060 (−0.568–0.444)			−0.034 (−0.505–0.446)
Myelin density				**p < 0.001**		**p < 0.001**
				0.034 (0.015–0.054)		0.034 (0.014–0.054)
Cortical Aβ-plaques					p = 0.514	p = 0.817
					0.035 (−0.091– 0.152)	0.0123 (−0.112– 0.129)
Log Likelihood	−84.97	−83.02	−83.0	**−77.50**	−82.9	−77.50
AIC	181.94	180.03	181.98	**171.01**	181.70	174.98
BIC	195.43	195.77	199.96	**189.00**	199.69	197.47
Total R^2	0.25	0.32	0.34	**0.52**	0.29	0.51

Table 2 Associations between EPVS percentage area and total CAA. Results for the fixed effects of linear mixed effects models explaining percentage area of EPVS in the white matter of histopathological sections. Subject and cortical region (frontal, temporal, parietal, and occipital) were always set as random factors for the intercept. Data represent standardized fixed effects estimates with confidence intervals and statistical significance. Models were compared using likelihood ratio tests; smaller AIC and BIC values indicate a better model fit. Significant effects are highlighted in bold